Comparison of wave modeling methods in CFD solvers for ocean engineering applications

Zhaobin Li, Ganbo Deng, Patrick Queutey, Benjamin Bouscasse, Guillaume Ducrozet, Lionel Gentaz, David Le Touzé, Pierre Ferrant

Version of Record: https://www.sciencedirect.com/science/article/pii/S0029801819300423
Manuscript_94ceca31a17218dcf58d2a216f7d9e7e

Comparison of wave modeling methods in CFD solvers for ocean engineering applications

Zhaobin Li, Ganbo Deng, Patrick Queutey, Benjamin Bouscasse*, Guillaume Ducrozet, Lionel Gentaz, David Le Touzé, Pierre Ferrant

Ecole Centrale Nantes, LHEEA research department (ECN and CNRS), Nantes, France

Abstract

Numerical wave tanks rely on specific models to generate realistic wave condition, propagate accurately the waves in the domain, and absorb the reflected waves at the boundaries. In this paper, three wave modeling methods for two-phase CFD solvers are compared, including the Internal Wave Generator method, the Relaxation Zone method, and the Spectral Wave Explicit Navier Stokes Equations (SWENSE) method. The first two methods consist in generating and absorbing the waves in specific regions of the domain, while the third achieves a potential/viscous coupling in the entire domain. These methods, implemented either in *OpenFOAM* or in *ISIS-CFD* are compared by simulating a fixed Catenary Anchor Leg Mooring (CALM) buoy in regular waves. The simulation results are compared with available experimental data obtained by a model test in the Ocean Engineering Tank of Ecole Centrale de Nantes. The comparison shows the efficiency and the accuracy of these waves modeling methods. A problem related to the turbulence modeling in two-phase flow is also remarked.

Keywords:
Wave modeling in CFD, Relaxation Zone, Internal Wave Generator, Potential/viscous flow coupling, SWENSE

1. Introduction

Reproducing the open sea environment in a finite domain is a common challenge faced by both physical and Numerical Wave Tanks (NWT) for ocean engineering applications. The key technique is to generate incident waves and to prevent the reflection at the domain boundaries at the same time.

A physical experimental wave tank usually generates waves with wavemakers and uses an absorption beach to prevent wave reflection on the other end.

In NWTs, reproducing a wavemaker using moving mesh and a wave-absorption beach is computationally expensive and thus is often replaced by numerical wave generation and absorption models. The simplest method is to use the incident wave velocity and the free surface elevation as boundary conditions. This kind of boundary allows incident waves to travel in and out but causes wave reflections when the real waves are different from the incident waves, e.g., diffracted waves by structures. Without proper treatments, large domains should be used to secure a time window long enough for data analysis before the reflected waves travel back (same as in physical wave tanks, but with a high computational cost).

Efforts in two major directions to overcome this difficulty can be found in the literature.

The first direction focuses on developing generation-absorption boundary conditions, aiming to use the boundary to generate incident waves and absorb the diffracted waves at the same time, for example, the weakly reflecting boundary condition proposed by Petit et al. (1995) and the active absorption boundary condition proposed by Higuera et al. (2013). However, these methods use linear superposition to combine the incident and the diffracted waves and are thus limited to small diffraction cases.

Methods in the second direction treat the wave generation and the absorption problems separately.

The Internal Wave Generator (IWG) method generates incident waves in a specific zone inside the computational domain and absorbs all the outgoing waves with sponge-layers on boundaries. The IWG method is originally proposed by Larsen and Dancy (1983) in a Boussinesq equation model, and has been extended to Navier-Stokes models by adding source terms either in the mass conservation equation (Lin and Liu, 1999) or in the momentum equation (Choi and Yoon, 2009) to generate unidirectional regular or irregular waves. Chen and Hsiao (2016) and Ha et al. (2013) have enabled multi-directional wave generation by using two perpendicular IWG zones. The IWG is transparent to the flow, allowing any waves passing through the wavemakers without interference, so this is particularly good for cases with significant wave reflection, such as simulating wave shoaling and breaking on the beach (Lara et al., 2006) and waves interacting with structures, such as, wave energy converters (Schmitt and Elsaesser, 2015; López et al., 2014), floating offshore wind turbines (Calderer et al., 2018), etc.

Another widely used method is the Relaxation Zone (RZ) method. Differently from the IWG method where waves are generated anywhere in a zone inside the computational domain, the RZ method blends the numerical solution obtained by the

*Corresponding author
Email address: benjamin.bousscasse@ec-nantes.fr (Benjamin Bouscasse)

solver to a reference solution in a zone near the boundaries of the domain. The velocity and the free surface position computed are "relaxed" to an incident wave solution, this generates waves out of the RZs and also avoid outgoing waves being reflected. This method was initially used by Mayer et al. (1998) to only absorb outgoing waves by setting the incident solution to zero. After being extended for wave generation and implemented in OpenFOAM by Jacobsen et al. (2012), the RZ method is now widely used by the ocean and coastal engineering community. It has been applied to simulate regular and irregular wave propagation (Choi et al., 2018), wave breaking on a steep beach (Chella et al., 2015), and waves interacting structures, such as, substructures of offshore wind turbines (Paulsen et al., 2014a,b), wave energy converters (Kamath et al., 2015; Palm et al., 2016), coastal bridges (Seiffert et al., 2014; Hayatdavoodi et al., 2014), and ships (Seo et al., 2017).

Moreover, coupling viscous flow solver with potential wave theory is also used to model waves in NWTs, as in the Spectral Wave Explicit Navier-Stokes Equations (SWENSE) (Ferrant et al., 2003; Vukčević et al., 2016a; Li et al., 2018, 2019) method. The SWENSE method solves the incident wave propagation problem with fully non-linear potential wave models, and uses the CFD solver only to solve the complementary field. Since the incident waves are no more treated by the CFD solver, one needs only to prevent the complementary field (the diffraction, radiation, etc) from reflecting in the far-field. This can be easily achieved since the complementary waves decrease naturally as they travel away. An absorption approach may also be used to damp out the complementary waves in the far-field. This method has been successfully applied to simulate wave-structure interactions, such as ships in waves (Luquet et al., 2003; Reliquet et al., 2013) and vertical cylinder in waves (Vukčević et al., 2016b; Li et al., 2017).

Miquel et al. (2018) compared the active wave absorption method (from the first category) and the RZ method (from the second category) and concluded that the latter is more effective.

The present work aims to compare the wave modeling methods from the second category, namely, the IWG, the RZ, and the SWENSE methods, for ocean engineering applications. The three methods are implemented in a similar numerical framework: using the Finite Volume Method and simulating the two-phase air water flow by the Volume of Fluid (VOF) technique (Hirt and Nichols, 1981). The IWG method is implemented in ISIS-CFD[1], a CFD code developed at Ecole Centrale de Nantes and distributed commercially by NUMECA International as a part of the FINE/Marine computing suite[2]; the RZ and the SWENSE methods are implemented in foamStar, developed by Ecole Centrale Nantes and Bureau Veritas, based on OpenFOAM[3], a widely used open source CFD software package. This comparison is achieved by studying a real ocean engineering application case, concerning a fixed Catenary Anchor Leg Mooring (CALM) buoy exposed to regular incident waves in open sea. The experiment carried out in the ocean engineering tank at Ecole Centrale de Nantes is also provided for the comparison. The wave generation and absorption performance and the computational efficiency of the three methods are mainly concerned. A problem related to the turbulence modeling in two-phase flow is also remarked.

The paper is structured as follows. After this introduction, the theory part describes the governing equations of NWTs and the principles of the three wave generation and absorption methods. Sect. 3 provides information of the model test in the experimental wave tank. Sect. 4 includes the numerical study of the same case, the data analyses, and the comparison. The conclusion is given in the end.

2. Theory

This section provides the theory about establishing a NWT using two-phase CFD solvers. In Sect. 2.1, the basic governing equations of two-phase flow is given. In Sect. 2.2, the theory of the IWG method, the RZ method, and the SWENSE method is described.

2.1. Governing equations

In classical ocean engineering application, the fluid is assumed as incompressible and the surface tension is ignored. In this condition, the two-phase air-water flow in a NWT is modeled with the Reynolds Averaged Navier-Stokes Equations (RANSE), as follows:

$$\nabla \cdot \mathbf{u} = 0 \tag{1}$$

$$\frac{\partial (\rho \mathbf{u})}{\partial t} + \nabla \cdot (\rho \mathbf{u} \otimes \mathbf{u}) = -\nabla p + \rho \mathbf{g} + \nabla \cdot \left(\mu_{\text{eff}} \left(\nabla \mathbf{u} + \nabla \mathbf{u}^T \right) \right) \tag{2}$$

where $\mathbf{u}$ is the velocity vector field, ρ is the density of the fluid, p is the pressure field, $\mathbf{g}$ is the gravitational acceleration vector, and μ_{eff} is the effective dynamic viscosity defined as $\mu_{\text{eff}} = \mu + \rho \nu_t$, with μ the fluid dynamic viscosity and ν_t the turbulent eddy viscosity. $k - \omega$ SST model is used to determine the turbulence eddy viscosity (Menter, 1994). The fluid properties ρ and μ remain to be determined with interface capturing techniques, such as the VOF method (Hirt and Nichols, 1981) in the present implementations.

The VOF method defines a scalar field α representing the volume fraction of water in a cell. This field is equal to 1 when the cell is fully occupied by water, and is equal to 0 when the cell is full of air. Cells on the interface have $0 < \alpha < 1$. The fluid properties are defined with an interpolation between water and air using α as weight.

$$\rho = \alpha \rho_{\text{water}} + (1 - \alpha) \rho_{\text{air}} \tag{3}$$

$$\mu = \alpha \mu_{\text{water}} + (1 - \alpha) \mu_{\text{air}} \tag{4}$$

The VOF field is advected by the velocity field $\mathbf{u}$, as follows,

$$\frac{\partial \alpha}{\partial t} + \nabla \cdot (\mathbf{u} \alpha) = 0 \tag{5}$$

These equations are the common and fundamental part of two-phase VOF solvers and are implemented in ISIS-CFD.

[1] https://lheea.ec-nantes.fr/software-and-patents/isis-cfd-193387.kjsp
[2] https://www.numeca.com/product/finemarine
[3] http://www.openfoam.com

In foamStar, the momentum equation (Eqn. 2) is expressed in a slightly different form as follows,

$$\frac{\partial(\rho\mathbf{u})}{\partial t}+\nabla\cdot(\rho\mathbf{u}\otimes\mathbf{u}) = -\nabla p_{\mathrm{d}}-\mathbf{g}\cdot\mathbf{X}\nabla\rho+\nabla\cdot\left(\mu_{\mathrm{eff}}\left(\nabla\mathbf{u}+\nabla\mathbf{u}^{T}\right)\right) \quad (6)$$

where p_{d} is the dynamic pressure defined as $p_{\mathrm{d}} = p + \rho\mathbf{g}\cdot\mathbf{X}$, and $\mathbf{X} = (x, y, z)$ is the vector field of the cell center coordinates. Eqns. (2) and (6) are fully equivalent.

The VOF transport equation in foamStar also contains a small modification, as follows

$$\frac{\partial\alpha}{\partial t} + \nabla\cdot(\mathbf{u}\alpha) + \nabla\cdot(\mathbf{u}_{\mathrm{r}}\alpha(1-\alpha)) = 0 \quad (7)$$

Compare to Eqn. (5), the extra term represents an artificial compression to keep the interface sharp (Rusche, 2003).

2.2. Wave generation and absorption methods

2.2.1. IWG

The IWG method produces waves in a specific region inside the computational domain by adding a momentum source function in the governing equations. The implementation in ISIS-CFD is inspired by the method of Choi and Yoon (2009). A momentum source term is added in Eqn. (2). The modified momentum equation reads,

$$\frac{\partial(\rho\mathbf{u})}{\partial t} + \nabla\cdot(\rho\mathbf{u}\otimes\mathbf{u}) = -\nabla p + \rho\mathbf{g} + \nabla\cdot\left(\mu_{\mathrm{eff}}\left(\nabla\mathbf{u}+\nabla\mathbf{u}^{T}\right)\right) + r\rho\mathbf{a}_{I} \quad (8)$$

where $r\rho\mathbf{a}_I$ is the extra momentum source term calculated using incident wave kinematics. r is a scalar field that is equal to one inside the wave generation zone and to zero elsewhere, as shown in Fig. 1(a).

At the outlet boundary, a damping zone is applied to damp the waves to zero with numerical wave damping techniques.

2.2.2. RZ

The RZ approach (Jacobsen et al., 2012) is used together with wave generating and absorbing boundary conditions. NWTs using such boundary conditions alone suffer from the reflection problem when the simulated waves and the imposed incident waves are different at the boundary. To avoid such differences, RZs are added (see Fig. 1(b)) to gradually blend the computed value to the target value and force them to match at the boundary. The relaxed velocity and VOF fields in these regions are defined as a linear combination of the CFD solution and the target incident wave value, as follows:

$$\alpha_{\mathrm{relax}} = \omega\alpha_{\mathrm{I}} + (1-\omega)\alpha \quad (9)$$

$$\mathbf{u}_{\mathrm{relax}} = \omega\mathbf{u}_{\mathrm{I}} + (1-\omega)\mathbf{u} \quad (10)$$

where the variables without subscripts denote the solution of CFD solver and the subscript I denotes the incident wave values. In foamStar, the incident waves are defined by an external wave solver based on fully non-linear potential theory (Rienecker and Fenton, 1981; Ducrozet et al., 2019, 2012, 2016). ω is a space-dependent weight function chosen here as:

$$\omega = 1 - 3d^2 + 2d^3 \quad (11)$$

where d is the normalized distance in the RZ defined as the distance to the boundary divided by the length of the RZ (Monroy et al., 2016).

This blending procedure is applied at the end of each time step after a converged solution has been obtained. The relaxed values are then used in the further simulation. The pressure field is not relaxed, since it is obtained directly from the Poisson equation in the incompressible flow case.

This technique is used to generate incident waves at the inlet of the CFD domain, and can also prevent wave reflections at the boundary by letting the incident part of the waves go out of the domain and absorbing the other parts with the RZ. A thorough study on the optimal parameter setup can be found in the work of Choi et al. (2018).

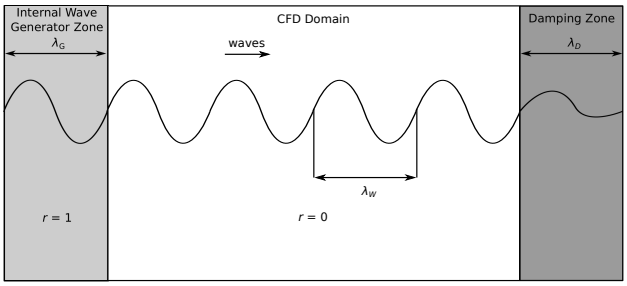

(a) Internal wave generator (IWG) method

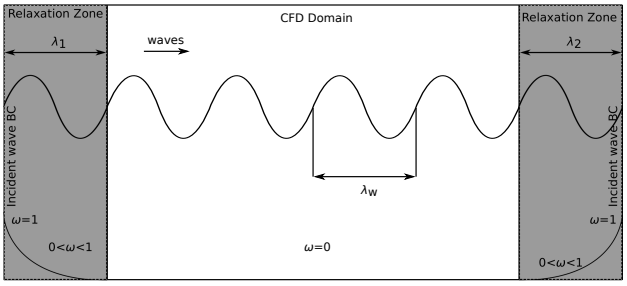

(b) Relaxation zone (RZ) method

Figure 1: Wave generation and absorption techniques

2.2.3. SWENSE

The SWENSE method (Ferrant et al., 2003) is a specific method designed to solve the wave-structure interaction problem using a potential/viscous flow coupling approach. It treats the wave-structure interaction problem by decomposing the total fields into: i) the incident part, and ii) the complementary part. The incident part describes the incident wave propagation in the computational domain without the structure; the complementary part represents the diffracted, radiated waves, and viscous effects. This decomposition is illustrated by Fig. 2. The decomposition is applied in the entire computational domain, no specific wave generation or absorption zone is defined as in the IWG and the RZ.

The two decomposed parts are treated separately.

The incident wave part is addressed by non-linear potential flow theory, under the inviscid and irrotational flow assumption and solved by spectral wave models. Regular incident

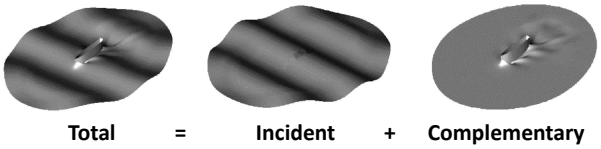

Figure 2: The SWENSE method decomposes the total field into an incident and a complementary part

waves are solved by the stream function wave theory (Rienecker and Fenton, 1981; Ducrozet et al., 2019), while irregular incident waves are solved with High-Order Spectral (HOS) method (Ducrozet et al., 2012, 2016).

The complementary part is treated by a viscous CFD solver. The governing equations of the complementary field are derived using the following idea: a variable χ (velocity, pressure) in Navier-Stokes equations (Eqns. 1 and 2) is decomposed into an incident variable χ_I and a complementary variable χ_C, as follows,

$$\chi = \chi_\mathrm{I} + \chi_\mathrm{C} \tag{12}$$

The incident variable χ_I represents the inviscid flow and is described by Euler equations. The governing equations of χ_C are mathematically derived by substituting Eqn. (12) into the Navier-Stokes equations (Eqns. 1 and 2) and simplifying them by Euler equations.

The original SWENSE method proposed by Ferrant et al. (2003) was made for single-phase solvers. It has been extended for two-phase CFD solvers in two recent works using different decomposition strategies. In the first work (Vukčević et al., 2016a,b), the SWENSE decomposition is applied only to the velocity field, leaving the entire pressure field to be solved by the viscous solver. In contrast, in the second work (Li et al., 2018, 2019), the SWENSE decomposition is applied to both the velocity and pressure fields. This more complete incident and complementary decomposition leads to less solution effort of the viscous solver. For this reason, the method in the second work is used in the present comparison.

The governing equations of the complementary fields read:

$$\nabla.\mathbf{u}_\mathrm{C} = 0 \tag{13}$$

$$\begin{aligned}&\frac{\partial \mathbf{u}_\mathrm{C}}{\partial t} + \mathbf{u}_\mathrm{C}.\nabla\mathbf{u}_\mathrm{C} + \mathbf{u}_\mathrm{C}.\nabla\mathbf{u}_\mathrm{I} + \mathbf{u}_\mathrm{I}.\nabla\mathbf{u}_\mathrm{C} \\ &= -\frac{\nabla p_\mathrm{C}}{\rho} - \frac{p_\mathrm{I}}{\rho_\mathrm{I}}\frac{\nabla\rho}{\rho} + \frac{\nabla\cdot\left(\mu_\mathrm{eff}\left(\nabla\mathbf{u}_\mathrm{C} + \nabla\mathbf{u}_\mathrm{C}^\mathrm{T}\right)\right)}{\rho}\end{aligned} \tag{14}$$

where $\rho_\mathrm{I} = \rho_\mathrm{water}$ is the water density, and p_I is the incident wave pressure provided by nonlinear potential theory. All the incident fields are extended to the viscous solver's computational domain. After solving the complementary field, the total field is reconstructed to obtain the final solution.

The merit of such decomposition is on the mesh requirement regarding the incident wave propagation. This one can be loosened since the incident wave information is explicitly known. A high mesh density is only necessary near the structure to solve the complementary field with a high level of accuracy.

The boundary condition of the complementary field at far-field boundary is defined to be zero. To ensure the complementary field vanish at far-field and to prevent its reflection, the outgoing complementary waves are either absorbed with coarse mesh or with RZs in the far-field zone.

3. Experimental study

The experimental study deals with a fixed CALM buoy (Rousset and Ferrant, 2005) in regular incident waves. The complexity of the geometry and of the flow represents a realistic ocean engineering application case, thus this study is suitable for comparing the different NWT models.

3.1. Experimental setup

The experiment has been conducted in the ocean engineering basin of ECN, which is rectangular and is 50m long, 30m wide, and 5m deep. One side of the tank is equipped with a segmented wavemaker, composed of 48 hinged flaps distributed over the width of the basin. Each flap is controlled separately. The wave generator system is equipped with an active wave absorption control feature. The opposite end of the basin is equipped with a passive wave breaking beach to prevent wave reflections. The side walls are reflective.

The geometry of the CALM buoy contains a truncated cylinder and a thin skirt near the bottom to provide additional heave damping force through vortex shedding, as shown in Fig. 3 and Tab. 1. In the experiment, the buoy is captured by a tripod and fixed at its design draft position. The center of the buoy locates on the basin's center-line and is 17.19m away from the wavemaker.

Uni-directional regular incident waves are used in this case. The wave parameters are provided in Tab. 2.

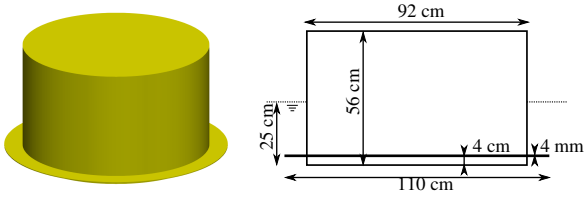

Figure 3: CALM buoy geometry

Geometry Parameter	Value (m)
Height overall	0.560
Draft	0.250
Buoy radius	0.460
Skirt radius	0.550
Skirt thickness	0.004
Bottom to mid-skirt distance	0.040

Table 1: Geometry parameters of the CALM buoy model

Parameter	Value
Period (T)	1.80 s
Height (H)	0.16 m
Depth (h)	5.00 m
Steepness (ka)	0.10
Relative water depth (kh)	6.20

Table 2: Target incident wave information

3.2. Data measurement and analysis

3.2.1. Data measurement

Wave forces and moments on the buoy are measured by a 5D-dynamometer (Mz is not measured). The free surface elevations are measured at four positions with resistance wave gauges. The data is acquired at 100Hz.

Three probes are located near the structure (see Fig. 4). Probe No.4 is located at 8m aside from the buoy and 17.19m away from the wavemaker to indicate the far-field wave information.

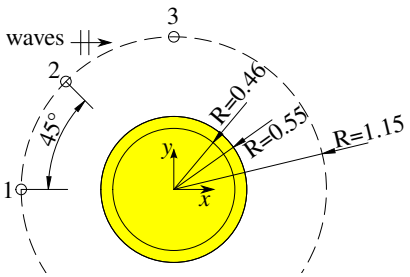

Figure 4: Wave probes near the buoy (top view)

3.2.2. Sliding window Fourier transform

The amplitudes of the zeroth (the mean value), the first and the second harmonic components of the measurement are obtained by the sliding window Fourier transform.

The sliding windows have a size equal to one wave period ($T = 1.8s$), the time increment between two windows is $\Delta t = 0.01T$. After such a transform, the amplitudes are recorded in function of time. Their time-averaged values and the standard deviations can be calculated in a chosen analysis zone.

3.2.3. Non-dimensionalization

The data is non-dimensionalized to take into account the probable discrepancies between the target and the measured incident waves. Such discrepancies are related to the use of a linear transfer function for the control of the wavemaker.

Figure 5 shows the free surface elevation measured by wave probe 4 (η_4), together with its first harmonic amplitude ($\eta_4^{(1)}$) extracted with the sliding window Fourier transform.

Ideally, its amplitude should remain constant and be equal to that of the target incident wave, if i) the wave generation and absorption are perfect and ii) this position is not affected by the diffracted waves. However, the measured wave amplitude contains several variations (see Fig. 5(b)), which indicates that the above assumptions are not fully satisfied. Such variations are interpreted as:

(A) At $t \approx 45$s, the arrival of the wave front: where small amplitudes waves are followed by steeper waves before the amplitude becomes nearly constant.

(B) At $t \approx 55$s, the arrival of diffracted waves: at first the diffracted waves from the buoy reach the probe; several periods later the waves get reflected at the side wall travels back and reach the probe again;

(C) At $t \approx 85$s, the arrival of reflected waves from the absorbing beach.

As a result, only the interval after the peak A and before the reflection B corresponds to the pure incident waves generated by the wavemaker at this probe. The measured wave height (crest to trough) in this interval is:

$$H_{\mathrm{m}} \pm \sigma_{H_{\mathrm{m}}} = 0.152\mathrm{m} \pm 0.0015\mathrm{m}$$

where H_{m} is the mean value and $\sigma_{H_{\mathrm{m}}}$ is the standard deviation. It is worth noting that the measured mean wave height H_{m} is slightly smaller than 0.16m, the target value.

In wave tank experiments, this difficulty in generating the exact target incident waves is overcome by converting the raw experimental data to non-dimensional values with a correction taking the measured incident wave information into account.

The non-dimensional wave forces are defined as

$$F_{\mathrm{nondim}} = \frac{F}{A_{\mathrm{m}} k \rho g V} \tag{15}$$

where F is the measured force, A_{m} is the measured amplitude, k is the wave number, and V is the immersed volume. The measured wave amplitude A_{m} is defined as

$$A_{\mathrm{m}} = \frac{1}{2} H_{\mathrm{m}} \tag{16}$$

The non-dimensional wave elevation is defined as

$$\eta_{\mathrm{nondim}} = \frac{\eta}{A_{\mathrm{m}}} \tag{17}$$

with η the measured free surface elevation.

3.2.4. Wave forces and free surface elevations

The first harmonic amplitudes of horizontal force and vertical forces (dimensionless values) are shown in Fig. 6.

Similarly as for the incident wave measurement, the three variations are also observed in the force amplitudes:

(A) At $t \approx 45$s, the arrival of the wave front;

(B) At $t \approx 65$s, the arrival of reflected diffracted waves from side wall;

(C) At $t \approx 85$s, the arrival of reflected waves from the beach.

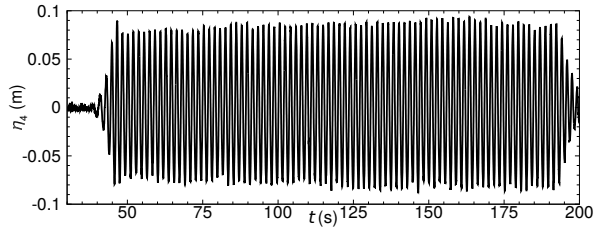

(a) Time history

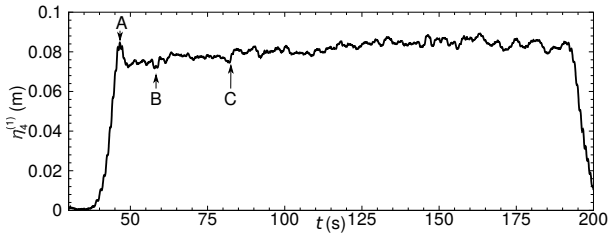

(b) First harmonic amplitude

Figure 5: Free surface elevation at probe No.4 in the experiment

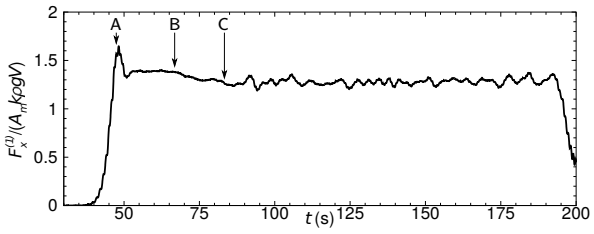

(a) Horizontal force

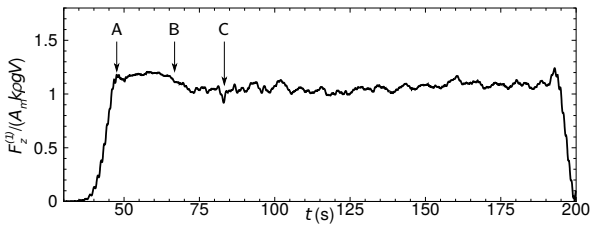

(b) Vertical force

Figure 6: The first harmonic amplitude of the wave force in the experiment

Component	Non dimensional amplitude		
	$\overline{x}$	σ_x	$\sigma_x/\overline{x}$
$F_x^{(1)}$	1.388	0.014	1%
$F_z^{(1)}$	1.185	0.016	1%
$\eta_1^{(1)}$	1.220	0.014	1%
$\eta_2^{(1)}$	1.194	0.012	1%
$\eta_3^{(1)}$	1.028	0.012	1%
$F_x^{(2)}$	0.176	0.008	5%
$F_z^{(2)}$	0.015	0.006	40%
$\eta_1^{(2)}$	0.065	0.007	11%
$\eta_2^{(2)}$	0.040	0.012	30%
$\eta_3^{(2)}$	0.035	0.008	23%
$F_x^{(0)}$	0.065	0.003	5%

Table 3: Experimental results

It is worth noting that the variation (B) happens about 10 seconds later for the force than that for the wave elevation at probe 4, since only the reflection caused by the side walls has an influence on the force and these waves need more time to propagate back to the center of the basin.

To obtain final results describing the true response to the incident waves, only data in the effective time window (after the peak A and before the variation B, where the amplitudes are almost constant) are used.

The experimental results are summarized in Tab 3. In the table, the superscript i represents the ith harmonic component. The results of first harmonics are given in the first place, followed by the second harmonics. The zeroth harmonic amplitude, representing the drift force, is also provided in the end. For each component, the mean value ($\overline{x}$) corresponds to the time-averaged value during the zone of analysis and the standard deviations (σ_x) include already the error on the incident waves in the non-dimensionalization. The relative standard deviation ($\sigma_x/\overline{x}$) represents the difficulty to obtain a precise result.

In this experiment, all the first harmonic amplitudes have relative standard deviations about 1%, showing a good data quality. However, the second harmonics are more difficult to obtain and contain larger relative standard deviations, since the mean values are much smaller. Only the horizontal force ($F_x^{(2)}$) has a fairly small standard deviation of about 5%. The zeroth harmonic amplitude of the horizontal force ($F_x^{(0)}$) has also a relative standard deviation of about 5%.

4. Numerical Study

This section reproduces the wave tank experiment using the three NWTs to compares the three wave modeling methods. The following features are considered:

- the accuracy;
- the computational efficiency;
- the wave generation and absorption ability.

The section begins by introducing the CFD solvers implementing the three wave modeling methods, and continues with

a description of the numerical setup. The numerical results and the discussions are presented in the end.

4.1. CFD solvers

The wave generation and absorption methods presented in Sect. 2.2 are implemented in two-phase CFD solvers. The IWG method is implemented with ISIS-CFD, while the RZ method and the SWENSE method are implemented in foamStar. Both ISIS-CFD and foamStar are based on the second-order accurate Finite Volume method. Unstructured polyhedral mesh with co-located variable arrangement is used. The governing equations are solved with the SIMPLE algorithm (Ferziger and Peric, 2012). The free surface is treated with the VOF method (Hirt and Nichols, 1981).

foamStar is based on interDyMFoam, the native OpenFOAM solver for incompressible two-phase flow. The solver's main structure is maintained; only slight modifications are made to implement the wave generation and absorption methods. Details can be found in Monroy et al. (2016) for the RZ implementation and in Li et al. (2018, 2019) for the SWENSE method.

4.2. Numerical setup

Two types of mesh are used in this test case. One is rectangular and the other is cylindrical, as shown in Figs. 7 and 8.

The rectangular configuration is normally used by most numerical wave tanks because its uniform and regular mesh is usually more accurate for the incident wave propagation.

The cylindrical configuration has fine cells only near the structure and coarse mesh in the far-field. This mesh arrangement contains a lower number of cells while keeping the density near the structure the same as in the rectangular configuration. It is consequently often more efficient. However, due to the coarse mesh in the far field, this configuration is not suitable to simulate wave propagation using classical Navier-Stokes models. But this configuration is compatible with the SWENSE method and shows its best performance, since the SWENSE method only need to solve the complementary fields, which is located close to the structure (in the zone with high mesh density).

In both configurations, the origin of the coordinate system is located at the center of the buoy and on the free surface at rest. The x axis points to the wave propagation direction, and z axis points upward. The depth of the computational domain is the same as in the experimental wave tank $z_{\text{min}} = -5\text{m}$. Only half of the domain is simulated by using a longitudinal symmetry plane.

The following part only details the spatial discretizations. The temporal discretization is set to have 360 time steps per wave period, which is considered to be fine enough according to a separate study (Choi et al., 2018).

4.2.1. Rectangular configuration

The rectangular configuration in Fig. 7 has Cartesian far-field mesh. Unstructured refined mesh is used locally near the structure to fit the geometry (see Fig. 9).

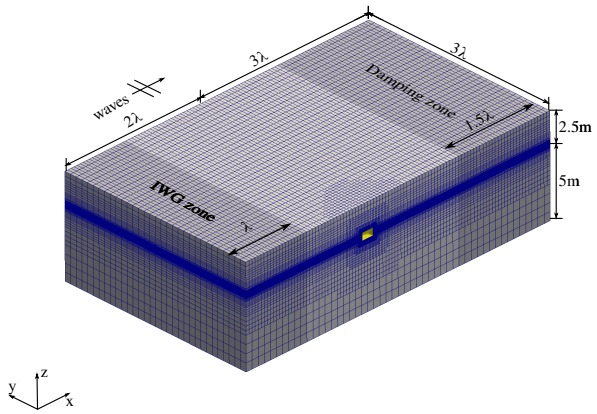

(a) IWG method

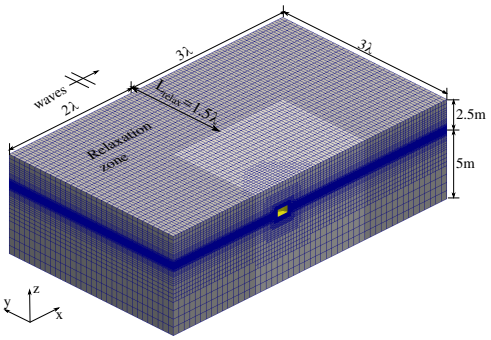

(b) RZ and SWENSE method

Figure 7: Rectangular mesh configurations

Three meshes with different far-field mesh densities: 20x, 40x, and 80x are used to compare the three models on their spatial discretization requirement. The number 20, 40, and 80 signify the number of cells per wavelength (λ) along the x direction. The far-field meshes are the only difference. The mesh density near the buoy is kept invariant and is assumed to be adequate to capture the flow details.

The mesh information is detailed in Tab. 4, where $\lambda = 5.05\text{m}$ and $H = 0.16\text{m}$ are the target incident wave length and height. Please note that the vertical discretization is kept unchanged in the three configurations and is assumed to be enough. The transverse (y) direction is not varying simultaneously with cells in the x direction. Such a configuration is commonly used to reduce the number of cells in unidirectional regular wave simulations. It has a preference wave propagation direction along which the mesh is more refined than the other direction.

Mesh	$\lambda/\Delta x$	$\lambda/\Delta y$	$H/\Delta z$	Number of cells
20x	20	10	16	1.3 M
40x	40	10	16	1.5 M
80x	80	20	16	2.5 M

Table 4: Rectangular mesh information

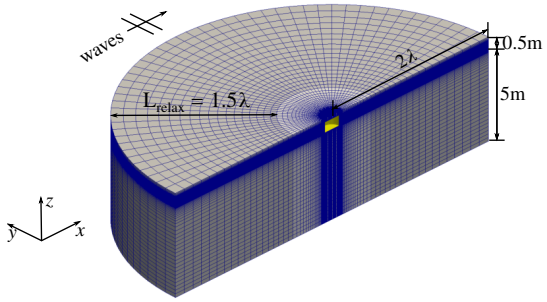

Figure 8: Cylindrical mesh configuration

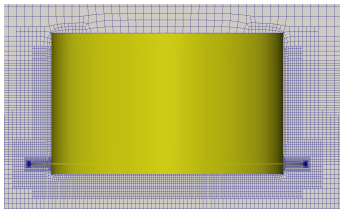

Figure 9: Local mesh refinement near the structure in the rectangular configuration (view from the symmetry plane)

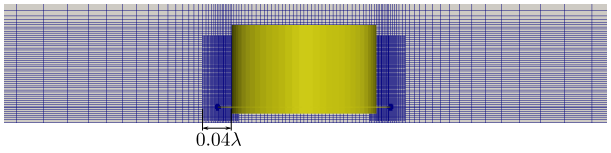

(a) C1 mesh

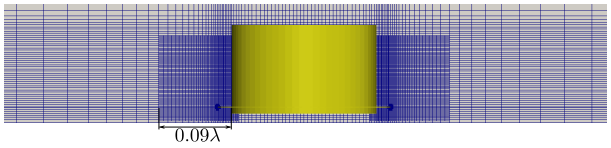

(b) C2 mesh

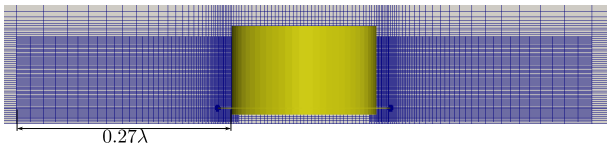

(c) C3 mesh

Figure 10: Local refinement regions near the buoy in the cylindrical configuration

4.2.2. *Cylindrical configuration*

As shown in Fig. 8, the mesh of the cylindrical configuration has fine cells near the center of the domain and coarse cells in the far-field. A local refinement is applied near the structure. The mesh density in this refinement zone is comparable to that of the rectangular configuration.

Using the cylindrical mesh with the SWENSE method assumes that the complementary fields (diffracted waves) need to be solved accurately only in a region close to the structure. This study analyzes the necessary size of this region.

Three meshes with different refinement zone sizes are used, as illustrated by Fig. 10 and referred to as C1, C2 and C3. Their details can be found in Tab. 5. In the table, Δr_{near} and Δr_{far} represent the radial size of the smallest and the largest cells respectively, r_{refine} denotes the width of the local refinement zone near the buoy.

Mesh	$\frac{\lambda}{\Delta r_{\text{near}}}$	$\frac{\lambda}{\Delta r_{\text{far}}}$	$\frac{180^o}{\Delta\theta}$	$\frac{H}{\Delta z}$	$\frac{r_{\text{refine}}}{\lambda}$	Cells
C1					0.04	0.72M
C2	500	10	48	16	0.09	0.82M
C3					0.27	1.01M

Table 5: Cylindrical mesh information

4.2.3. *Wave generation and absorption*

The wave generation and absorption methods used in the rectangular configuration are detailed as follows.

- The IWG method in ISIS-CFD: A wave generation zone of one wavelength long is set next to the inlet boundary ($x \in (x_{\min}, x_{\min} + \lambda)$), as shown in Fig. 7(a). The wave damping zone is 1.5 wavelength long, and is next to the outlet boundary ($x \in (x_{\max} - 1.5\lambda, x_{\max})$). The side wall is modeled as slip wall, since using damping zones near the side wall is not feasible. This configuration is very similar to the experimental condition. Reflection from the side wall is expected.

- The RZ method in foamStar uses incident wave boundary condition at the inlet, the outlet and the side wall. Three RZs with 1.5 wavelength long are used next to these boundaries ($x \in (x_{\min}, x_{\min} + 1.5\lambda)$ and $x \in (x_{\max} - 1.5\lambda, x_{\max})$ and $y \in (y_{\max} - 1.5\lambda, y_{\max})$), as shown in Fig. 7(b). This setup avoids the reflections at any domain boundary to simulate an open sea condition.

- The SWENSE method in foamStar does not need wave generation zone, but uses RZs to prevent the reflections of complementary waves. These zones are set in the same way as in the RZ method to simulate an open sea condition.

For the cylindrical configuration, the SWENSE method in foamStar uses a RZ of 1.5 wavelength long around the far-field boundary to simulate an open sea condition, as shown in Fig. 8.

The stream function wave theory (Rienecker and Fenton, 1981; Ducrozet et al., 2019) is used to calculate the target incident waves as shown in Tab. 2.

4.3. *Results*

Same information is collected in the numerical study as in the experiment. The raw data is non-dimensionalized and processed with sliding windows Fourier transform in the same way as in the experiment. For simplicity, only the analysis procedure for the horizontal wave force is detailed here. The complete results are provided in Tab. 6, and further compared in Figs. 15 and 16.

It is worth noting that the non-dimensionalization in the numerical study uses the target incident value and not the measured value, so to see the errors in the wave propagation.

4.3.1. IWG in ISIS-CFD

The simulation using the IWG method starts with calm water condition at $t = 0$. The waves are generated in the wave making zone and propagates in the NWT. Figure 11 plots the horizontal wave force during the first 10 wave periods and its first harmonic amplitude. The three different curves represent the results using different discretizations.

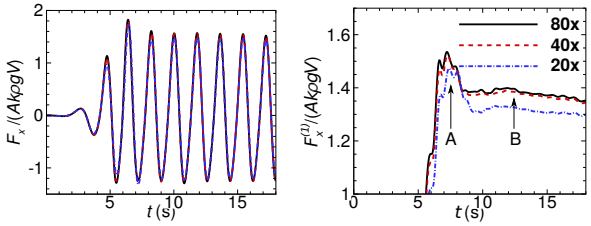

(a) Time history (b) First harmonic amplitudes

Figure 11: Horizontal wave force: internal wave generation method in ISIS-CFD

From Fig. 11(b), it is observed that the force amplitudes are not constant, but with two obvious variations. Similar to the experiment, the horizontal wave force exhibits a peak after the arrival of the wave front (point A). It is also worth noting that the wave force amplitudes begins to decrease at $t \approx 12$s (point B). Although this decrease is similar to the experiment, it is not due to the side wall reflection, since the reflected waves need more time to travel back. This decrease is caused by the damping zone at the outlet, the distance of which is only 1.5 wavelength away from the buoy. The traveling time estimated with the wave group velocity is equal to $10.8s$. For this reason, only a short time window after the peak A and before the reflection B can be used for data analysis.

Besides, the wave forces show a converging trend with the mesh refinement. The results using the 20x mesh is about 10% smaller than the two close results with the 40x and 80x meshes.

4.3.2. RZ in foamStar

At the beginning of the simulation, the incident waves are initialized everywhere in the entire computational domain. Such initial condition is necessary to ensure the compatibility of the flow in the pure CFD zone and in the RZs (blending to incident wave).

The results of such initial condition is shown by the peak A in Fig. 12(b)), which corresponds to the impact caused by the sudden appearance of the buoy in the incident waves. The following trough corresponds to the establishment of the diffracted waves. Note that the amplitude curve starts one period later compared to the time history, since the sliding window Fourier transform uses one wave period as the window length.

After point A ($t = 1.8$s), the force amplitudes remain almost constant for a short interval. It may be interpreted as the response to the incident waves initialized at the beginning of the simulation. Then force amplitudes decrease between point A and point B ($t \approx 7$s). This decrease suggests that the waves generated at the inlet boundary become smaller while propagating in the CFD domain due to numerical errors in the wave modeling method. This loss of wave amplitude is more severe with the coarse mesh (20x) than with the fine mesh (80x), but the duration of such a decrease is the same for the three meshes, which is approximately equal to the time to propagate information from the inlet boundary to the structure at the wave group velocity.

After point B, the results become almost constant and correspond to the converged results with each discretization. Compared to the IWG result, the duration of the stable result is longer, so it offers a longer zone to extract the final results.

The results in different meshes have larger discrepancy compared with the IWG's results in ISIS-CFD.

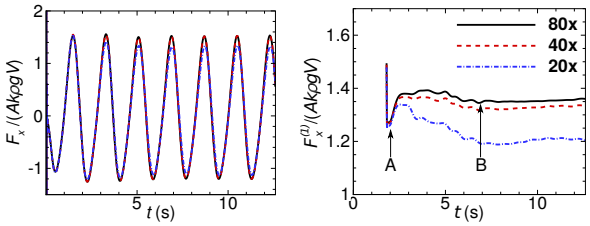

(a) Time history (b) First harmonic amplitudes

Figure 12: Horizontal wave force: RZ method in foamStar

4.3.3. SWENSE in foamStar

Figures 13 and 14 plot the horizontal force obtained with the rectangular and the cylindrical mesh configurations.

The initial condition in the SWENSE simulation is the same as the RZ method, i.e., the incident waves exist everywhere. Thus, the wave force at the beginning of the simulation is similar to that of the RZ method near point A.

The point B in Figs. 13(b) and 14(b) are plotted at the same position as in Fig. 12(b), i.e., at $t = 7$s, since the information propagation time should be identical. However, the decrease of the force amplitudes between A and B is much smaller than that of the RZ method, showing that the loss of wave amplitude caused by the SWENSE method is also smaller than the RZ method.

After point B the simulation results become almost constant, offering a long zone of analysis to extract the final result.

In Fig. 13, the cylindrical mesh simulations show very close results. The force amplitudes increase slightly when enlarging the size of refinement zone near the structure. It suggests that solving the complementary field accurately in different spatial extents has a slight influence. The quantitative study of this problem will be given in Sect. 4.3.4 and the compromise between the accuracy and the computational cost using the SWENSE method will be further addressed in Sect. 4.4.1.

Moreover, in Fig. 14, the difference between mesh configurations are very small, revealing that the far-field spatial discretization has only minor influence on the accuracy of wave

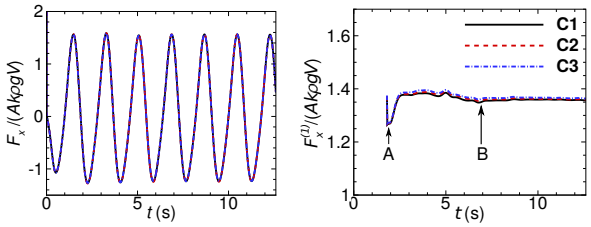

(a) Time history (b) First harmonic amplitudes

Figure 13: Horizontal wave force: SWENSE method in foamStar with the cylindrical mesh

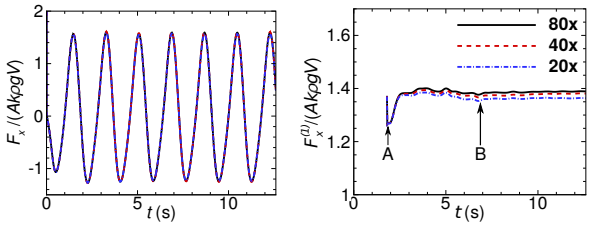

(a) Time history (b) First harmonic amplitudes

Figure 14: Horizontal wave force: SWENSE method in foamStar with the rectangular mesh

force calculation.

4.3.4. *Summary of the results*

The simulation results are detailed in Tabs. 6 and 7, including the first two harmonic amplitudes of the wave force (horizontal and vertical) and of the wave amplitudes at the three probes close to the buoy. The zeroth harmonic amplitude of the horizontal wave force is also provided. In the table, the mesh names are followed by the number of cells to indicate the computational cost.

These data are obtained with the sliding window Fourier transform, in the same way as in the experiment. Only the numerical results inside the exploitable zone are used for the data processing, to exclude the transitional regime at the beginning and the influence of the wave reflections (in the IWG case). For example, in the interval wave generation case in Fig. 11(b), the result after peak A and before B is used; in the RZ method and the SWENSE method, the results after point B are used (see Figs. 12-14).

For each result, the mean value is provided and followed by its standard deviation to give an indication of the periodical uncertainty.

Before going into details, the tables show a general good agreement between the experimental data and the numerical results on the mean values, especially when the finest mesh (80x) is used. This agreement indicates that all the three wave modeling methods are able to simulate correctly the waves and the interaction with the structure. With respect to the standard deviation, the results of the IWG method in ISIS-CFD have the largest deviations, which are comparable with that in experimental data. The results of RZ method and the SWENSE method in foamStar have smaller deviations, suggesting a more stable simulation results, which is in agreement with the observation from Figs. 11-14.

Among these quantities, the first harmonics are one or two orders of magnitudes larger than the second harmonics and thus describe the majority of the physical phenomenon. Besides, they contain relatively small standard deviations, showing better data quality. The second harmonics, especially that of the vertical force has much smaller mean values and much larger standard deviations. For this reason, the comparison shall concentrate on the first harmonics forces, which are the main interest from the engineering point of view.

For this reason, the comparison is at first conducted for the first harmonics of the horizontal and vertical forces, in Fig. 15. The first harmonic amplitude of the free surface elevation at probe 1 is also shown. In each figure, the vertical axis denotes the non-dimensional amplitude. The horizontal axis describes the mesh information in ascending order of number of cells. The mean experimental data is plotted with a black solid line, which is encompassed by a red region covering one standard deviation above and below. The mean values of the simulation results are described by the bars. The error bars represent one standard deviation above and below the mean values.

In Fig. 15(a), the first harmonic amplitudes of the horizontal wave forces ($F_x^{(1)}$) are plotted. All the three methods achieve good results compared to the experimental data when the finest discretization (80x) is used, but their accuracy varies significantly on coarser meshes. With 80x mesh, the difference to the experimental data is smaller than 3% for the foamStar-RZ, while the results of ISIS-CFD-IWG and the foamStar-SWENSE are very close to the experimental data. When meshes become coarser, the behavior of the three wave modeling methods become different. ISIS-CFD-IWG and foamStar-SWENSE can still produce results with errors smaller than one standard deviation, with 40x mesh, while the foamStar-RZ are about 5% smaller. When the mesh becomes even coarser, only the results of foamStar-SWENSE show no obvious degradation of accuracy. For the foamStar-RZ and ISIS-CFD-IWG, the wave force decreases when enlarging the far-field cell size. This decrease is most due to the numerical diffusion errors induced by the mesh in the incident wave propagation. The IWG method and RZ methods rely on the CFD solver to calculate the incident wave propagation and thus require fine cells everywhere in the domain. In contrast, the incident waves of the SWENSE method are solved with external potential flow solvers and are not affected by the CFD mesh. As a result, the SWENSE method is the least sensitive to the quality of far-field mesh.

In Figs. 15(b) and 15(c), the first harmonic amplitudes of the vertical force ($F_z^{(1)}$) and the free surface elevation at probe 1 (η_1) reveal similar results with the horizontal force, i.e., the three methods show close and the most accurate results with 80x mesh, but the SWENSE method is the least sensitive to the far-field mesh quality. However, for the vertical force ($F_z^{(1)}$), an obvious larger discrepancy between the numerical results and the experimental data is observed. Even with the finest mesh, this difference still remains and exists for all the three meth-

Non-dimensional Amplitude		$F_x^{(1)}$	$F_z^{(1)}$	$\eta_1^{(1)}$	$\eta_2^{(1)}$	$\eta_3^{(1)}$
Experiment		1.388 ± 0.014	1.185 ± 0.016	1.210 ± 0.014	1.194 ± 0.012	1.028 ± 0.012
ISIS-CFD-IWG	20x (1.3M)	1.323 ± 0.017	1.072 ± 0.020	1.158 ± 0.014	1.139 ± 0.013	0.966 ± 0.019
	40x (1.5M)	1.376 ± 0.003	1.109 ± 0.019	1.200 ± 0.015	1.181 ± 0.012	0.997 ± 0.014
	80x (2.4M)	1.385 ± 0.004	1.118 ± 0.021	1.201 ± 0.017	1.189 ± 0.014	1.009 ± 0.013
foamStar-RZ	20x (1.3M)	1.204 ± 0.008	1.020 ± 0.010	1.056 ± 0.005	1.049 ± 0.005	0.918 ± 0.013
	40x (1.5M)	1.328 ± 0.004	1.076 ± 0.004	1.169 ± 0.003	1.161 ± 0.007	0.983 ± 0.004
	80x (1.4M)	1.352 ± 0.002	1.109 ± 0.004	1.193 ± 0.003	1.178 ± 0.004	1.000 ± 0.002
foamStar-SWENSE	C1 (0.72M)	1.358 ± 0.002	1.129 ± 0.002	1.196 ± 0.003	1.180 ± 0.001	1.013 ± 0.001
	C2 (0.82M)	1.362 ± 0.001	1.126 ± 0.002	1.197 ± 0.002	1.181 ± 0.001	1.013 ± 0.001
	C3 (1.0M)	1.367 ± 0.001	1.129 ± 0.002	1.198 ± 0.002	1.183 ± 0.001	1.020 ± 0.001
	20x (1.3M)	1.363 ± 0.001	1.137 ± 0.002	1.196 ± 0.001	1.181 ± 0.001	1.023 ± 0.001
	40x (1.5M)	1.379 ± 0.002	1.143 ± 0.002	1.208 ± 0.001	1.192 ± 0.001	1.030 ± 0.001
	80x (2.4M)	1.388 ± 0.001	1.148 ± 0.002	1.214 ± 0.002	1.197 ± 0.001	1.037 ± 0.001

Table 6: Comparison between numerical results and experimental data: first harmonics

Non-dimensional Amplitude		$F_x^{(0)}$	$F_x^{(2)}$	$F_z^{(2)}$	$\eta_1^{(2)}$	$\eta_2^{(2)}$	$\eta_3^{(2)}$
Experiment		0.067 ± 0.003	0.176 ± 0.008	0.015 ± 0.006	0.064 ± 0.007	0.022 ± 0.012	0.038 ± 0.008
ISIS-CFD-IWG	20x (1.3M)	0.056 ± 0.009	0.130 ± 0.013	0.032 ± 0.011	0.076 ± 0.015	0.032 ± 0.009	0.080 ± 0.022
	40x (1.5M)	0.061 ± 0.005	0.195 ± 0.012	0.022 ± 0.009	0.073 ± 0.010	0.055 ± 0.010	0.071 ± 0.014
	80x (2.4M)	0.062 ± 0.006	0.019 ± 0.015	0.028 ± 0.010	0.058 ± 0.010	0.033 ± 0.015	0.048 ± 0.004
foamStar-RZ	20x (1.3M)	0.053 ± 0.002	0.130 ± 0.004	0.017 ± 0.003	0.057 ± 0.003	0.037 ± 0.003	0.036 ± 0.004
	40x (1.5M)	0.070 ± 0.002	0.165 ± 0.002	0.009 ± 0.005	0.056 ± 0.002	0.034 ± 0.003	0.038 ± 0.003
	80x (1.4M)	0.070 ± 0.001	0.166 ± 0.001	0.011 ± 0.005	0.059 ± 0.002	0.034 ± 0.002	0.043 ± 0.002
foamStar-SWENSE	C1 (0.72M)	0.067 ± 0.001	0.175 ± 0.001	0.018 ± 0.003	0.067 ± 0.002	0.043 ± 0.002	0.051 ± 0.001
	C2 (0.82M)	0.065 ± 0.001	0.178 ± 0.002	0.016 ± 0.003	0.068 ± 0.002	0.043 ± 0.002	0.052 ± 0.001
	C3 (1.0M)	0.065 ± 0.001	0.175 ± 0.003	0.015 ± 0.003	0.068 ± 0.002	0.038 ± 0.002	0.050 ± 0.002
	20x (1.3M)	0.069 ± 0.001	0.177 ± 0.001	0.014 ± 0.002	0.066 ± 0.002	0.044 ± 0.002	0.041 ± 0.001
	40x (1.5M)	0.070 ± 0.001	0.184 ± 0.001	0.011 ± 0.002	0.062 ± 0.002	0.040 ± 0.002	0.039 ± 0.001
	80x (2.4M)	0.070 ± 0.001	0.185 ± 0.001	0.011 ± 0.002	0.062 ± 0.002	0.039 ± 0.002	0.040 ± 0.001

Table 7: Comparison between numerical results and experimental data: mean force and second harmonics

ods. Provided that the heave damping skirt mainly influences the vertical wave force, it is possible that the local refinement near the skirt (identical in all the meshes) is not enough to capture accurately the complex vortex shedding phenomenon.

The zeroth harmonic and the second harmonic of the horizontal force is about 5% and 10% to the first harmonic force. These values can give a more detailed comparison of the accuracy. Moreover, the zeroth harmonic is of engineering interest since it corresponds to the drift force of the waves. Figure 16 provides such a comparison. The SWENSE method still shows a good accuracy on both quantities, regardless the mesh used, while the loss of amplitudes is also obvious in the results of the foamStar-RZ and ISIS-CFD-IWG with mesh 20x, due to the numerical damping caused by large mesh size in the far field. The foamStar-RZ achieves good results with fine meshes (40x and 80x), while the ISIS-CFD-IWG underestimates the drift force and has larger periodical uncertainty in its result.

4.4. Discussion

4.4.1. Efficiency of the models

The results reveal that each wave modeling method achieves its best accuracy with the finest discretization (80x mesh). However, the use of coarse mesh in the far-field has different influence on their accuracy. The SWENSE method is able to use much coarser mesh by giving little concession on the accuracy and thus is the most efficient wave modeling method among the three, and is very advantage in cases where the efficiency is more emphasized than the absolute accuracy,

To confirm that, we compare the efficiency of the three models according to their mesh requirement to reach a same level of accuracy.

Taking the first harmonic amplitude of the horizontal wave force as an example: if set an accuracy tolerance of 3% ($1.35 < F_x^{(1)} < 1.43$), then ISIS-CFD-IWG requires the 40x mesh with 1.5 million cells to meet the criteria; foamStar-RZ requires the 80x mesh with 2.5 million cells; while foamStar-SWENSE is able to achieve the same level of accuracy with the coarsest C1 mesh with only 0.72 million of cells.

The efficiency enhancement in the SWENSE method is credited to the use of the potential/viscous coupling approach, so that accurate incident waves are independent of the CFD mesh, only the complementary field needs to be solved.

Moreover, this study confirms that the complementary fields need only to be solved accurately in a close vicinity of the structure, so that a small local refinement zone near the structure with coarse mesh in the far-field is able to produce good results: the cylindrical mesh with a local refinement of 0.04 incident wave length around the structure (C1) is enough to achieve a good estimation of horizontal wave force with -2.3% error compared to the experimental data. Although enlarging this local refinement zone to 0.27 wave length wide (C3) can reduce the error to -1.7%, using larger refinement zone is not always necessary if the efficiency is more emphasized than the accu-

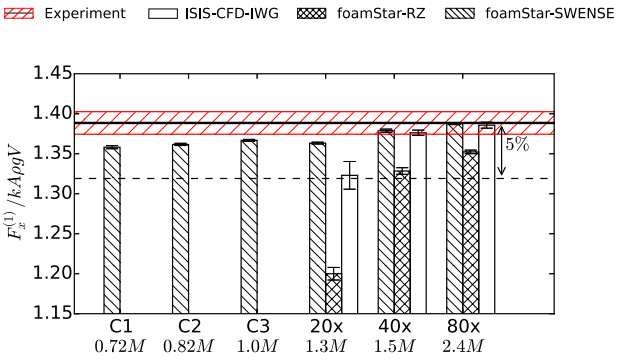

(a) Horizontal force: 1st Harmonic Amplitudes

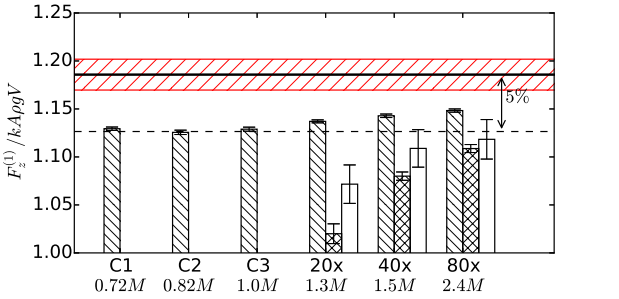

(b) Vertical force: 1st Harmonic Amplitudes

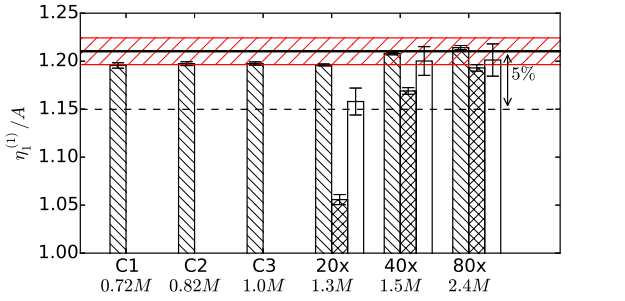

(c) Wave elevation at probe 1: 1st Harmonic Amplitudes

Figure 15: Comparison of simulation results: first harmonics of the wave forces and the free surface elevation

racy.

To ensure the accuracy of the simulation, especially to validate the result of SWENSE on the coarse mesh, the flow details of the simulation are compared. The IWG method uses the medium mesh 40x; the RZ method uses the finest mesh 80x; the SWENSE method uses the coarsest mesh 20x. With such discretizations, all methods should have a same level of accuracy. Figure 17 plots the Q-criterion and the pressure fields obtained by the three methods, showing a good agreement.

4.4.2. Wave reflection prevention ability

The wave reflection is prevented using two strategies in the present study.

- Full absorption condition: damping zones are used to absorb the entire wave trains at the outlet boundary, as in the IWG method and in the experiment.

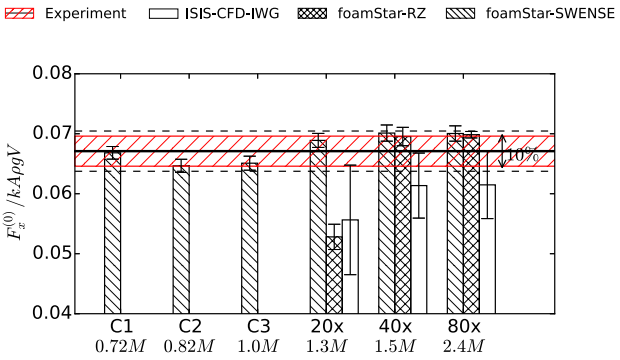

(a) Horizontal force: mean force

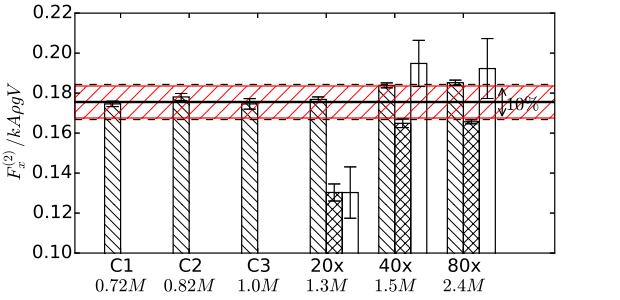

(b) Horizontal force: 2nd Harmonic Amplitudes

Figure 16: Comparison of simulation results: the mean horizontal wave force and the second harmonic of the horizontal force

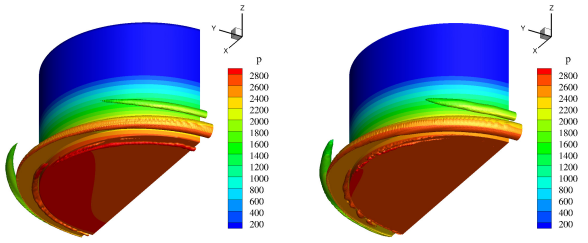

(a) ISIS-CFD-IWG 40x (b) foamStar-RZ 80x

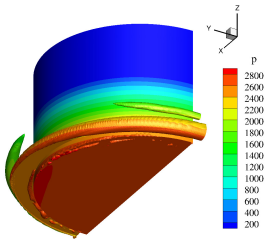

(c) foamStar-SWENSE 20x

Figure 17: Comparison of the iso-surfaces of Q-criterion = 50 and the pressure field when a wave crest passes the buoy

- Diffraction absorption condition: this condition allows the incident waves to leave the computational domain and absorb the diffracted waves only, as in the RZ method and in the SWENSE method.

It is observed that the diffraction absorption condition prevents better wave reflection, comparing with the full absorption condition.

For example, when the full absorption condition is used, both the experiment and numerical methods show difficulty in damping out the full wave trains at the end of the domain. Reflected waves travel back to the structure and affect the results (see point C in Fig. 6 and point B in Fig. 11(b)). As a result, the exploitable window for the data analysis is reduced. A secondary effect of the full absorption condition is that it can not be used to prevent side wall reflections. In the present study, the numerical simulation with the IWG method is not long enough to make this phenomenon appear, but the experimental data confirms the necessity of avoiding side wall reflections.

The RZ method and the SWENSE method both use the diffraction absorption condition at all domain boundaries. With both methods, no apparent wave reflections are observed, the simulations are more stable and provide longer exploitable time for the data analysis.

Inspired by the RZ method, forcing zones are added to the IWG method to achieve the diffraction absorption condition. The forcing zone is similar to the RZ, but it uses a momentum source in the RANS equations to force the CFD solution equal to the incident wave solution, and thus it provides the absorption of the diffracted waves. In Fig. 18 the results of IWG using forcing zones at side walls and the outlet are plotted by red dash lines and compared to the original method shown by black lines. The forcing zones avoid the wave reflections and show a much more stable result.

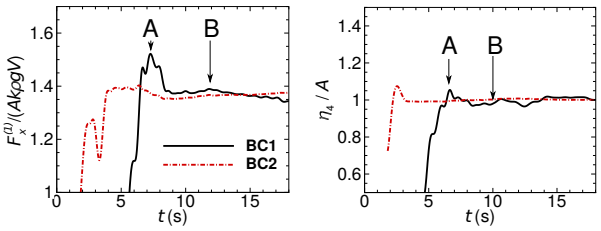

(a) Horizontal wave force (b) Wave amplitude at probe 4

Figure 18: Influence of the absorption boundary condition for the IWG method: BC1 wave damping at outlet, and BC2 forcing zones at outlet and at side wall

4.4.3. Remark on the turbulence model in two-phase flow

In the present numerical study, the standard $k-\omega$ SST turbulence model is selected to calculate the eddy viscosity in the RANS equations. However, an excessive wave damping and a wave force diminishing are observed with the RZ method implemented in OpenFOAM. Figure 19 shows the 0th and 1st harmonic amplitudes of the horizontal wave force. A loss in amplitude is observed from $t = 15s$. This problem is purely numeric and limits the effective time window to analyze the physics.

This problem has been reported in the literature (Devolder et al., 2017) on using RANS model for two-phase flow simulations and it is attributed to the limitation of the present turbulence models, which are mostly derived and tuned for single-phase flows. These models are usually not adequate to consider the discontinuity of physics near the free surface and create excessive and nonphysical turbulent eddy-viscosity, which leads to the wave damping. This problem is often severe in a wave-structure interaction problem without forward speed, since the turbulent viscosity always remains in the computational domain.

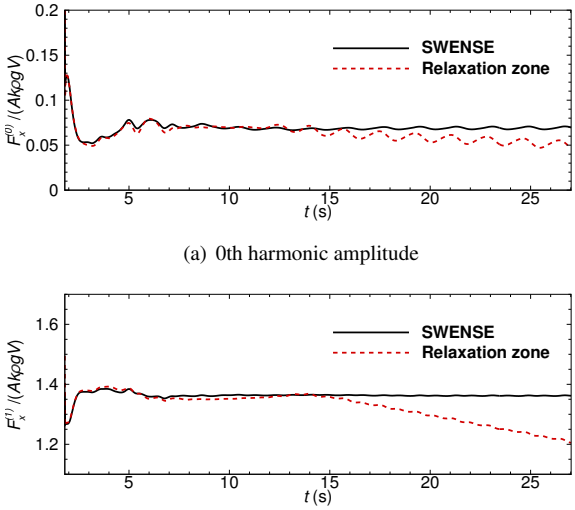

(a) 0th harmonic amplitude

(b) 1st harmonic amplitude

Figure 19: Horizontal wave force result in a long time simulation

Figure 20 shows the turbulent viscosity (ν_t) at $t = 1T$ and $t = 15T$ in the simulation with the RZ method. After one wave periods, the turbulent viscosity appears not only close to structure but also in the far-field. The far-field turbulence is created near the free surface, which is shown as a white line, due to the interface discontinuity. The maximum ν_t has an order of $10^{-3}\mathrm{m}^2/\mathrm{s}$ at $t = 1.8\mathrm{s}$. At the end of the simulation, the turbulent viscosity has a much larger value (order of $10^{-1}\mathrm{m}^2/\mathrm{s}$) due to the accumulation and appears in a larger zone.

The result of the SWENSE method is not affected by this problem. Despite using the same turbulence model, the wave force amplitudes are maintained constant even after a long simulation time. This has to be credited to the potential/viscous coupling used in SWENSE method, so that the viscous effects is only applied to the complementary field and does not affect the incident waves.

5. Conclusion

The present work compared three wave modeling methods in two-phase CFD solvers: the IWG method in ISIS-CFD, the RZ method and the SWENSE method in foamStar. The accuracy and the performance of these methods are compared by simulating a fixed CALM buoy in regular waves and compared with experiments.

On the accuracy side, all the three methods are able to achieve accurate comparison with the experiment when the

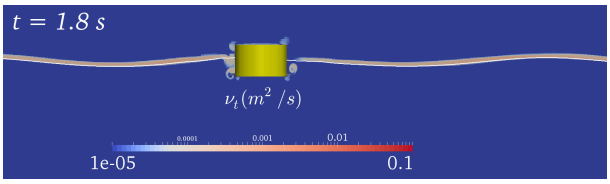

(a) One wave period after the simulation

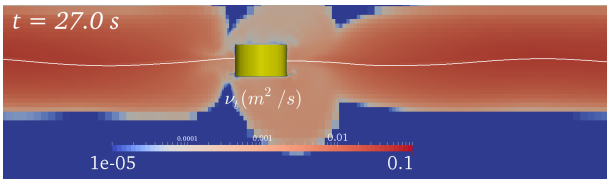

(b) 15 wave periods after the simulation

Figure 20: Turbulent viscosity in the computational domain (view from the symmetry plane). Note that the color map uses a logarithmic scale. The free surface is shown as a white line.

mesh is fine enough to propagate the incident waves accurately. Compared to the SWENSE method in foamStar, the IWG method in ISIS-CFD and the RZ method in foamStar show more dependency on fine meshes to obtain accurate results. Only the SWENSE method in foamStar still obtain good results with coarse far-field mesh.

On the performance side, the SWENSE method in foamStar is the most efficient. It is able to achieve a significant gain in efficiency with a tiny concession on the accuracy, by using coarse mesh in the far-field. For a same level of accuracy, the SWENSE method requires only about 25% cells compared to the RZ method, with both methods implemented in OpenFOAM.

The diffraction absorption condition prevents better wave reflection than the full absorption condition. The RZ and the SWENSE method in foamStar, using the diffraction absorption condition, are able to prevent reflections at all the domain boundaries, and thus provide more stable result and longer time window for the data analysis. The full absorption method (damping), used by the IWG method in ISIS-CFD and the experiment, creates larger reflection at the outlet and is inapplicable for side wall absorption. Using forcing zones is able to achieve the diffraction absorption condition in the IWG method.

A last remark shows the $k-\omega$ SST turbulence model is not adapted for two-phase flow simulation in standard RANSE solvers, since it causes excessive numerical damping of incident waves. The use of the potential/viscous coupling method as the SWENSE method is able to alleviate this problem and maintain good simulation results for longer simulation time.

6. Acknowledgments

This work has been performed in the framework of the Chaire Hydrodynamique et Structure Marines CENTRALE NANTES - BUREAU VERITAS. Part of this work was granted access to the HPC resources of IDRIS and CINES under the allocations 2018-A0032A01308 made by GENCI (Grand Équipement National de Calcul Intensif). The first author acknowledges China Scholarship Council (CSC) for the financial support for his PhD study.

References

Calderer, A., Guo, X., Shen, L., Sotiropoulos, F., 2018. Fluid–structure interaction simulation of floating structures interacting with complex, large-scale ocean waves and atmospheric turbulence with application to floating offshore wind turbines. Journal of Computational Physics 355, 144–175.

Chella, M. A., Bihs, H., Myrhaug, D., Muskulus, M., 2015. Breaking characteristics and geometric properties of spilling breakers over slopes. Coastal Engineering 95, 4–19.

Chen, Y.-L., Hsiao, S.-C., 2016. Generation of 3D water waves using mass source wavemaker applied to Navier-Stokes model. Coastal Engineering 109, 76–95.

Choi, J., Yoon, S. B., 2009. Numerical simulations using momentum source wave-maker applied to RANS equation model. Coastal Engineering 56 (10), 1043–1060.

Choi, Y., Bouscasse, B., Seng, S., Ducrozet, G., Gentaz, L., Ferrant, P., 2018. Generation of regular and irregular waves in Navier-Stokes CFD solvers by matching with the nonlinear potential wave solution at the boundaries. In: 37th International Conference on Ocean, Offshore and Arctic Engineering. American Society of Mechanical Engineers.

Devolder, B., Rauwoens, P., Troch, P., 2017. Application of a buoyancy-modified k-ω SST turbulence model to simulate wave run-up around a monopile subjected to regular waves using OpenFOAM®. Coastal Engineering 125, 81–94.

Ducrozet, G., Bonnefoy, F., Le Touzé, D., Ferrant, P., 2012. A modified high-order spectral method for wavemaker modeling in a numerical wave tank. European Journal of Mechanics-B/Fluids 34, 19–34.

Ducrozet, G., Bonnefoy, F., Le Touzé, D., Ferrant, P., 2016. HOS-ocean: Open-source solver for nonlinear waves in open ocean based on High-Order Spectral method. Computer Physics Communications 203, 245–254.

Ducrozet, G., Bouscasse, B., Gouin, M., Ferrant, P., Bonnefoy, F., 2019. CNStream: Open-source library for nonlinear regular waves using stream function theory. arXiv preprint arXiv:1901.10577.

Ferrant, P., Gentaz, L., Alessandrini, B., Le Touzé, D., 2003. A potential/RANSE approach for regular water wave diffraction about 2-D structures. Ship Technology Research 50 (4), 165–171.

Ferziger, J. H., Peric, M., 2012. Computational methods for fluid dynamics. Springer Science & Business Media.

Ha, T., Lin, P., Cho, Y.-S., 2013. Generation of 3d regular and irregular waves using navier–stokes equations model with an internal wave maker. Coastal Engineering 76, 55–67.

Hayatdavoodi, M., Seiffert, B., Ertekin, R. C., 2014. Experiments and computations of solitary-wave forces on a coastal-bridge deck. part ii: Deck with girders. Coastal Engineering 88, 210–228.

Higuera, P., Lara, J. L., Losada, I. J., 2013. Simulating coastal engineering processes with OpenFOAM®. Coastal Engineering 71, 119–134.

Hirt, C. W., Nichols, B. D., 1981. Volume of fluid (VOF) method for the dynamics of free boundaries. Journal of Computational Physics 39 (1), 201–225.

Jacobsen, N. G., Fuhrman, D. R., Fredsøe, J., 2012. A Wave Generation Toolbox for the Open-Source CFD Library: OpenFoam®. International Journal for Numerical Methods in Fluids 70 (9), 1073–1088.

Kamath, A., Bihs, H., Arntsen, Ø. A., 2015. Numerical investigations of the hydrodynamics of an oscillating water column device. Ocean Engineering 102, 40–50.

Lara, J., Garcia, N., Losada, I., 2006. Rans modelling applied to random wave interaction with submerged permeable structures. Coastal Engineering 53 (5-6), 395–417.

Larsen, J., Dancy, H., 1983. Open boundaries in short wave simulations-a new approach. Coastal Engineering 7 (3), 285–297.

Li, Z., Bouscasse, B., Gentaz, L., Ducrozet, G., Ferrant, P., 2018. Progress in coupling potential wave models and two-phase solvers with the SWENSE methodology. In: 37th International Conference on Ocean, Offshore and Arctic Engineering. American Society of Mechanical Engineers.

Li, Z., Bouscasse, B., Gentaz, L., Ducrozet, G., Ferrant, P., 2019. Spectral Wave Explicit Navier-Stokes Equations for wave-structure interactions using two-phase Computational Fluid Dynamics solvers, submitted.

Li, Z., Gentaz, L., Ducrozet, G., Ferrant, P., 2017. Calculation of high-order wave loads on a vertical circular cylinder using the swense method. In: 32th IWWWFB.

Lin, P., Liu, P. L.-F., 1999. Internal wave-maker for Navier-Stokes equations models. Journal of waterway, Port, Coastal, and Ocean Engineering 125 (4), 207–215.

López, I., Pereiras, B., Castro, F., Iglesias, G., 2014. Optimisation of turbine-induced damping for an owc wave energy converter using a rans–vof numerical model. Applied Energy 127, 105–114.

Luquet, R., Gentaz, L., Ferrant, P., Alessandrini, B., 2003. Viscous flow simulation past a ship in waves using the swense approach. In: ONR Conference.

Mayer, S., Garapon, A., Sørensen, L. S., 1998. A fractional step method for unsteady free-surface flow with applications to non-linear wave dynamics. International Journal for Numerical Methods in Fluids 28 (2), 293–315.

Menter, F. R., 1994. Two-equation eddy-viscosity turbulence models for engineering applications. AIAA journal 32 (8), 1598–1605.

Miquel, A. M., Kamath, A., Alagan Chella, M., Archetti, R., Bihs, H., 2018. Analysis of different methods for wave generation and absorption in a cfd-based numerical wave tank. Journal of Marine Science and Engineering.

Monroy, C., Seng, S., Malenica, S., 2016. Développements et validation de l'outil CFD OpenFOAM pour le calcul de tenue à la mer. In: Proceedings of the 15th Journées de l'Hydrodynamique.

Palm, J., Eskilsson, C., Paredes, G. M., Bergdahl, L., 2016. Coupled mooring analysis for floating wave energy converters using cfd: Formulation and validation. International Journal of Marine Energy 16, 83–99.

Paulsen, B. T., Bredmose, H., Bingham, H. B., 2014a. An efficient domain decomposition strategy for wave loads on surface piercing circular cylinders. Coastal Engineering 86, 57–76.

Paulsen, B. T., Bredmose, H., Bingham, H. B., Jacobsen, N. G., 2014b. Forcing of a bottom-mounted circular cylinder by steep regular water waves at finite depth. Journal of fluid mechanics 755, 1–34.

Petit, H., Tönjes, P., Van Gent, M., Van Den Bosch, P., 1995. Numerical simulation and validation of plunging breakers using a 2D Navier-Stokes model. In: Coastal Engineering 1994. pp. 511–524.

Reliquet, G., Drouet, A., Guillerm, P.-E., Jacquin, E., Gentaz, L., Ferrant, P., 2013. Simulation of wave-body interaction using a single-phase level set function in the swense method. In: ASME 2013 32nd International Conference on Ocean, Offshore and Arctic Engineering. American Society of Mechanical Engineers.

Rienecker, M., Fenton, J., 1981. A Fourier approximation method for steady water waves. Journal of Fluid Mechanics 104, 119–137.

Rousset, J.-M., Ferrant, P., 2005. Model tests for Principia R&D. Tech. Rep. CTR1 - JIP Calm Buoy 2, Laboratoire de Mécanique des Fluides de l'Ecole Centrale de Nantes (UMR CNRS 6598).

Rusche, H., 2003. Computational fluid dynamics of dispersed two-phase flows at high phase fractions. Ph.D. thesis, Imperial College London (University of London).

Schmitt, P., Elsaesser, B., 2015. On the use of openfoam to model oscillating wave surge converters. Ocean Engineering 108, 98 – 104.

Seiffert, B., Hayatdavoodi, M., Ertekin, R. C., 2014. Experiments and computations of solitary-wave forces on a coastal-bridge deck. part i: Flat plate. Coastal Engineering 88, 194–209.

Seo, S., Park, S., Koo, B., 2017. Effect of wave periods on added resistance and motions of a ship in head sea simulations. Ocean Engineering 137, 309–327.

Vukčević, V., Jasak, H., Malenica, Š., 2016a. Decomposition model for naval hydrodynamic applications, Part I: Computational method. Ocean Engineering 121, 37–46.

Vukčević, V., Jasak, H., Malenica, Š., 2016b. Decomposition model for naval hydrodynamic applications, Part II: Verification and validation. Ocean engineering 121, 76–88.